electronics

MDPI

Article

High−Performance 4H−SiC UV p−i−n Photodiode: Numerical Simulations and Experimental Results

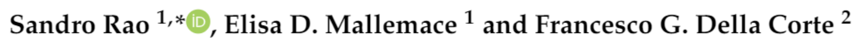

Sandro Rao [1,*], Elisa D. Mallemace [1] and Francesco G. Della Corte [2]

[1] Department DIIES, Mediterranea University, 89124 Reggio Calabria, Italy; elisa.mallemace@unirc.it
[2] Department DIETI, University of Naples Federico II, 80125 Naples, Italy; francescogiuseppe.dellacorte@unina.it
* Correspondence: sandro.rao@unirc.it

Abstract: In this work, the optical response of a high−performance 4H−SiC−based p−i−n ultraviolet (UV) photodiode was studied by means of an ad hoc numerical model. The spectral responsivity and the corresponding external photodiode quantum efficiency were calculated under different reverse biases, up to 60 V, and in the wavelength range from λ = 190 to 400 nm. The responsivity peak is R = 0.168 A/W at λ = 292 nm at 0 V and improves as bias increases, reaching R = 0.212 A/W at 60 V and λ = 298 nm. The external quantum efficiency is about 71% and 88%. The good quality of the simulation setup was confirmed by comparison with experimental measurements performed on a p−i−n device fabricated starting from a commercial 4H−SiC wafer. The developed numerical model, together with the material electrical and optical parameters used in our simulations, can be therefore explored for the design of more complex 4H−SiC−based solid−state electronic and optoelectronic devices.

Keywords: silicon carbide; numerical model; UV photodiode

Citation: Rao, S.; Mallemace, E.D.; Della Corte, F.G. High−Performance 4H−SiC UV p−i−n Photodiode: Numerical Simulations and Experimental Results. *Electronics* **2022**, *11*, 1839. https://doi.org/10.3390/electronics11121839

Academic Editor: Christos Volos

Received: 21 April 2022
Accepted: 7 June 2022
Published: 9 June 2022

Publisher's Note: MDPI stays neutral with regard to jurisdictional claims in published maps and institutional affiliations.

Copyright: © 2022 by the authors. Licensee MDPI, Basel, Switzerland. This article is an open access article distributed under the terms and conditions of the Creative Commons Attribution (CC BY) license (https://creativecommons.org/licenses/by/4.0/).

1. Introduction

Silicon Carbide (SiC), due to its excellent physical and electrical properties, has become a good candidate for high−power, high−temperature, and high−frequency applications [1]. More in general, its use is constantly growing in many electronic systems, above all when the external operating conditions become critical.

Light detection, in particular in the ultraviolet (UV) spectral range, has recently drawn attention in several application fields, from chemical and biological analysis, flame detection, to optical communications and astronomical studies [2]. Wide−bandgap semiconductors, in fact, thanks to the low intrinsic carrier concentration, have the advantage of an extremely low dark current, which can be many orders of magnitude lower than conventional silicon (Si)−based photodetectors [2].

During the past decade, high−performing 4H−SiC [3] and 6H−SiC [4,5] UV photodetectors have been more widely studied. Different structures have been proposed, such as p−i−n [6,7], Schottky [8], avalanche [9,10], and metal–semiconductor–metal (MSM) UV photodetectors [11].

Among these structures, p−i−n photodiodes are in principle of particular interest due to better reliability and stability also in high−thermal stress conditions, whereas Schottky−type SiC−based photodiodes' performances start to degrade at moderately high temperatures and become increasingly leaky as temperature increases [12]. Moreover, p−i−n photodetectors are intrinsically low−noise devices and exploit the expanded depletion region to enhance the collection efficiency and, therefore, the separation mechanism of the photogenerated carriers [13].

In this work, we present a high−performance 4H−SiC−based p−i−n UV photodiode. In particular, a numerical model for simulating the electro−optical (EO) outputs,

such as the responsivity (R) under different reverse biases and its corresponding external quantum efficiency (EQE), was developed. The finite−element method for semiconductor device simulation was particularized with the main EO physical parameters achieved through experimental studies on the same materials and device [14]. In such a way, the specific 4H−SiC properties were tuned, leading to a reliable numerical simulator whose results are in very good agreement with the experimental ones. In this sense, simulations and physics−based modelling represent critical tools to make sure that newly conceived technologies stand up to the requirements of the microelectronic industry.

2. Device Structure: The p−i−n Photodiode

The studied and experimentally characterized photodiode (Figure 1) is an integral part of a microchip processed by the CNR, Institute for Microelectronics and Microsystem of Bologna (Bologna, Italy) [15].

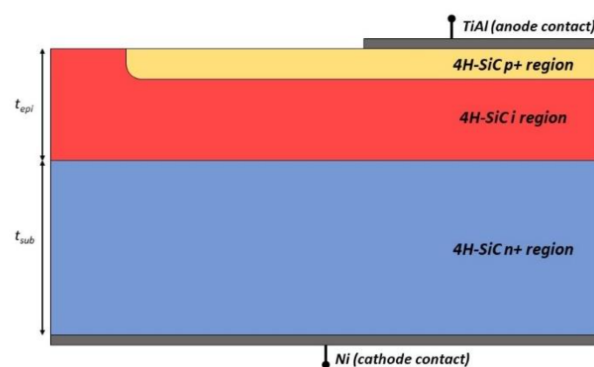

Figure 1. 4H−SiC p−i−n photodiode schematic cross−section, <x,y> plane. The slightly doped (n−type) 4H−SiC region is 16.5 μm thick. The simulated device is 1 μm thick along the orthogonal−to−the−plane z−direction. Figure is not in scale. t_{epi} is 16.5 μm, and t_{sub} is 300 μm thick.

The p−i−n diode was fabricated on an <0001> 8° off−axis 4H−SiC epitaxial wafer, 300 μm thick [16]. The starting n^+ planar substrate has a doping concentration of $N_{sub} = 5 \times 10^{19}$ cm^{-3}, whereas the slightly doped (n−type) epitaxial layer was 16.5 μm thick with a donor doping of $N_{epi} = 3 \times 10^{15}$ cm^{-3}. The implanted p−type anode region showed an aluminium (Al) concentration of 7×10^{19} cm^{-3} at the surface, with a profile edge located at ~0.2 μm and a tail crossing the constant epilayer doping at ~1.35 μm from the anode contact, as measured by Secondary Ion Mass Spectrometry (SIMS) measurements [17]. The Al−implanted doping concentration profile is schematically reported in Figure 2.

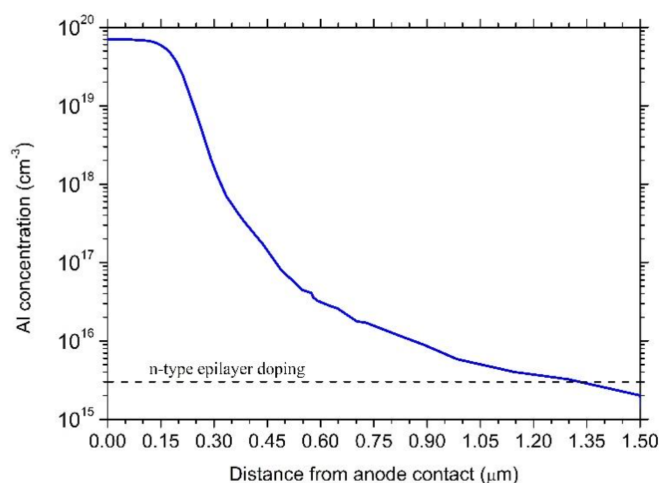

Figure 2. Secondary ion mass spectrometry profile of the Al−implanted doping concentration.

In our simulations, a length of 370 μm (x−direction) and a 1 μm width (z−direction) were set up. The anode contact circular area is 175 μm^2, while the cathode contact area is 370 μm^2. The main physical parameters for the three doped 4H−SiC regions are summarized in Table 1.

Table 1. 4H−SiC p−i−n regions' physical parameters.

4H−SiC	p^+	n^-	n^+
Doping (cm^{-3})	7×10^{19} (peak)	3×10^{15}	5×10^{19}
Thickness (μm)	See profile in Figure 2	16.5	300.0
Bandgap energy (eV)	3.26	3.26	3.26
Saturated velocity (cm^2/s)	2×10^7	2×10^7	2×10^7
Dielectric constant	9.66	9.66	9.66

This basic structure was simulated to calculate, firstly, the diode electrical characteristics also at different DC−bias conditions. Two− and three−dimensional modelling and simulation processes allowed obtaining a better understanding of the properties and physical behaviour of the Device Under Test (DUT). Moreover, the net charge generation due to incident light power, taking into account the charge transport and generation recombination mechanisms using the standard drift−diffusion transport equations coupled with Shockley–Read–Hall, Auger, and optical generation−recombination models was simulated.

3. Electro−Optical Numerical Model

The electrical simulations, performed at room temperature (T = 300 K), were based on the physical models describing mobility and carrier lifetime as a function of both doping concentration and temperature, apparent bandgap narrowing, incomplete ionization of dopants, impact ionization, Shockley–Read–Hall, and Auger recombination processes.

In particular, the bandgap narrowing dependence on temperature is defined by using the following expression:

$$E_g(T) = E_{g0} - \frac{\alpha T^2}{\beta + T} \tag{1}$$

where E_{g0} is the bandgap energy at T = 0 K and α and β are specific material coefficients equal for 4H−SIC, respectively, to -3.3×10^{-4} and 0 eV/K.

Moreover, when impurities are introduced into the semiconductor crystal, due to the wide bandgap of 4H−SiC, not all the doping atoms can be assumed as fully ionized. This depends on the impurity energy level and the lattice temperature. Using the Fermi–Dirac statistics, the ionized acceptor and donor impurity concentration, N_A^- and N_D^+, can be calculated with the following expressions [18]:

$$N_A^- = \frac{N_A}{1 + g_A e^{\frac{E_A - E_V}{k_B T}} e^{-\frac{E_F - E_V}{k_B T}}} \tag{2}$$

$$N_D^+ = \frac{N_D}{1 + g_D e^{\frac{E_C - E_D}{k_B T}} e^{\frac{E_F - E_C}{k_B T}}} \tag{3}$$

where N_A and N_D are the acceptor and donor impurity concentrations, respectively, g_A and g_D the corresponding ground−state degeneracy of the impurity level, equal for 4H−SiC to g_A = 4 and g_D = 2, E_A = 200 meV and E_D = 100 meV are the donor and acceptor energy levels, respectively, E_C and E_V are the bottom of the conduction band and the top of the valance band, respectively, E_F is the Fermi level, k_B is the Boltzmann constant, and finally, T is the temperature in Kelvin.

The 4H−SiC carrier mobility was modelled using the Caughey–Thomas analytic model. It specifies a low−field mobility, which in turn depends on the doping concentration and temperature. This correlation is defined by the following expression [19]:

$$\mu_{n,p} = \mu_{0n,p}^{min}\left(\frac{T_L}{300K}\right)^{\alpha_{n,p}} + \frac{\mu_{0n,p}^{max}\left(\frac{T_L}{300K}\right)^{\beta_{n,p}} - \mu_{0n,p}^{min}\left(\frac{T_L}{300K}\right)^{\alpha_{n,p}}}{1+\left(\frac{T_L}{300K}\right)^{\gamma_{n,p}}\cdot\left(\frac{N}{N_{n,p}^{crit}}\right)^{\delta_{n,p}}} \tag{4}$$

where N is the local (total) concentration of the ionized impurities, $\mu_{0n,p}^{min}$ and $\mu_{0n,p}^{max}$ are two reference parameters for the maximum and minimum mobility, $N_{n,p}^{crit}$ is the doping concentration at which the mobility is midway between the maximum and minimum values, and the terms $\alpha_{n,p}$, $\beta_{n,p}$, $\gamma_{n,p}$, and $\delta_{n,p}$ are fitting coefficients depending on the particular material considered. Table 2 summarizes the values adopted in our simulations.

Table 2. Carrier mobility parameters used for the Caughey–Thomas model.

Parameters	Electron	Hole
μ_0^{max} (cm^2/Vs)	950	125
μ_0^{min} (cm^2/Vs)	40	15.9
N^{crit} (cm^{-3})	2×10^{17}	1.76×10^{19}
α	−0.5	−0.5
β	−2.15	−2.15
$\delta = -\gamma$	0.76	0.76

The recombination model in 4H−SiC holds the deep levels in the bandgap by the Shockley–Read–Hall (*SRH*) model, physically implemented by the expression [20]:

$$R_{SRH} = \frac{pn - n_i^2}{\tau_p\left(n + n_i^2 e^{\frac{E_T - E_i}{k_B T}}\right) + \tau_n\left(p + n_i^2 e^{\frac{E_T - E_i}{k_B T}}\right)} \tag{5}$$

where n_i is the effective intrinsic carrier concentration, E_T is the energy level of the trap, E_i is the intrinsic Fermi level, and τ_n and τ_p are electron and hole lifetimes, respectively, calculated from (6):

$$\tau_{n,p} = \frac{\tau_{0n,p}}{1+\left(\frac{N}{N_{n,p}^{SRH}}\right)} \tag{6}$$

where $\tau_{0n,p}$ are process−dependent parameters, $N_{n,p}^{SRH}$ is a reference constant, and N is the total impurities' concentration of a device region.

Moreover, the *SRH* recombination is coupled with the band−to−band Auger recombination, according to the expressions:

$$R_{Auger} = (C_n n + C_p p)\left(np - n_i^2\right) \tag{7}$$

where C_n and C_p are the temperature−dependent Auger coefficients.

Table 3 summarizes all of the parameters used in our numerical simulator to model the Shockley–Read–Hall and Auger recombination phenomena.

Table 3. Parameters for the Shockley–Read–Hall and Auger recombination models.

Parameters	Electron	Hole
τ_0 (ns)	15	15
N_{SRH} (cm^{-3})	7×10^{16}	7×10^{16}

The impact ionization model used is that proposed by Selberherr. It is based on the following expression:

$$\alpha_{n,p} = A_{n,p}e^{-\left(\frac{B_{n,p}}{E}\right)^{\beta_{n,p}}} \quad (8)$$

where E is the electric field in the local current flow direction and $A_{n,p}$, $B_{n,p}$. and $\beta_{n,p}$ are material−dependent physical parameters.

As done for the electrical side, also the optical properties of 4H−SiC were defined both theoretically and experimentally. The complex refractive index, n + ik, is responsible for the photodiode spectral response; however, its value is not constant with wavelengths, and therefore, an ellipsometric analysis was performed in samples of 4H−SiC with a doping concentration similar to our quasi−intrinsic (i) p−i−n epilayer. The experimental plot, the wavelength−dependent real part of the refractive index (n), shown in Figure 3, was imported into our numerical model for wavelengths up to λ = 410 nm.

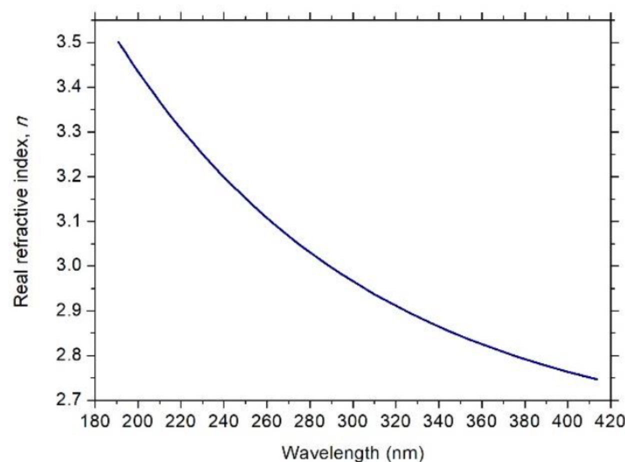

Figure 3. 4H−SiC real refractive index vs. wavelength measured through ellipsometry.

On the other hand, the imaginary part of the refractive index (k) is responsible for the light absorption in a medium. In order to determine its values for 4H−SiC at the wavelengths of our interest, we exploited a model based on experimental data of the dielectric function [21] available for a wide range of wavelengths. The extracted plot is reported in Figure 4 together with the imaginary refractive index suggested by Sridhara [22], for comparison. A good agreement between the two data sets is evident.

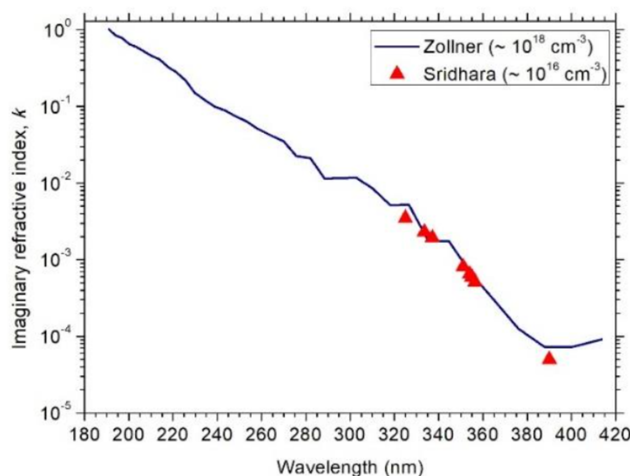

Figure 4. 4H−SiC imaginary refractive index (k) vs. wavelength.

4. Simulations and Experimental Results

Simulation results were compared to the photo−response characteristics of the experimental 4H−SiC UV p−i−n photodiode, characterized by the same geometrical dimensions and layer doping. All of the 4H−SiC physical parameters reported in the previous tables, and used in our developed numerical model, were tuned by comparison with these experimental results.

In our setup, UV radiation generated by a remotely controlled monochromator was used to illuminate the devices under test during the measurement of the J−V characteristics at different wavelengths in the range between λ = 190 nm and 400 nm, in steps of 5 nm. More details about the experimental results, up to 30 V DC in reverse bias applied between top (anode) and bottom (cathode) p−i−n diode contacts, and the used electro−optical setup, are reported in [3]; a schematic picture is however shown in Figure 5 together with the fabricated microchip, containing several photodiodes, bonded on a custom Printed Circuit Board (PCB), which allows a stable connection between devices and the measurement instrumentations.

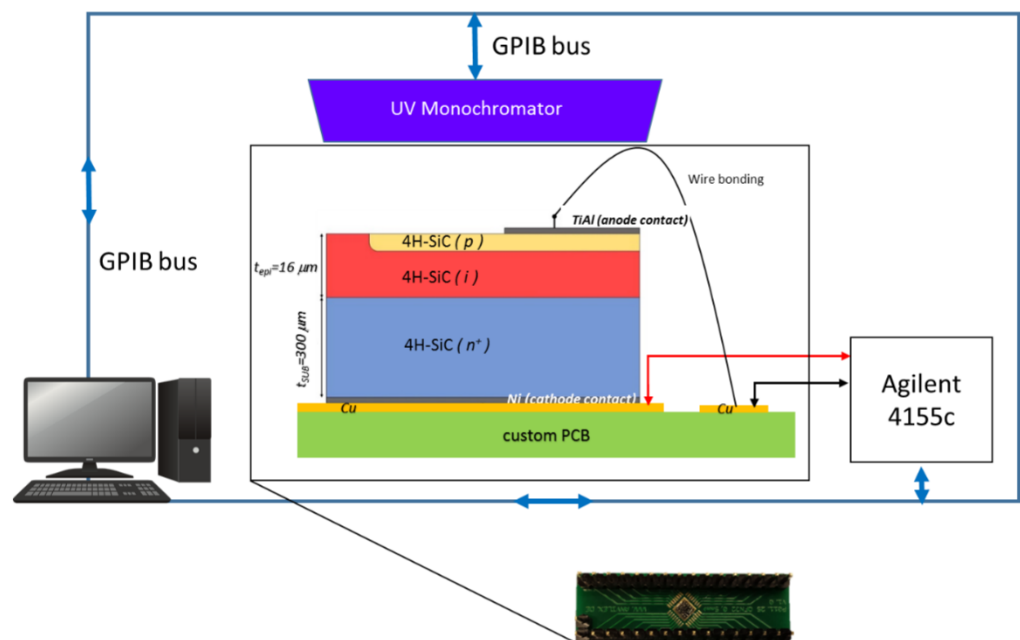

Figure 5. Schematic experimental setup and fabricated microchip bonded on a custom PCB for a stable remotely controlled measurement.

In [3], we demonstrated that at the wavelength of λ = 285 nm, the photo−response peak is R = 0.204 A/W at −30V, to our knowledge the best value if compared to those found in the literature, including Schottky photodiodes, p−i−n, and more sophisticated bipolar devices. Moreover, the calculated External Quantum Efficiency (EQE), defined as the photodiode's capability to convert an optical flux into an electrical energy, is 72.7%, the maximum value ever reported for UV photodiodes with no bias applied.

Here, we extend the previous experimental results [3] up to 60 V, in reverse bias, and the corresponding spectral responsivities of the 4H−SiC p−i−n photodiode, for both experiments and simulations, are compared to each other, from 0 V to 60 V in steps of 10 V, at the same wavelengths of interest.

As shown in Figure 6, the responsivity peak increases with the applied voltage. Moreover, the responsivity increases significantly up to 20 V, while this improvement becomes slower at biases beyond 30 V.

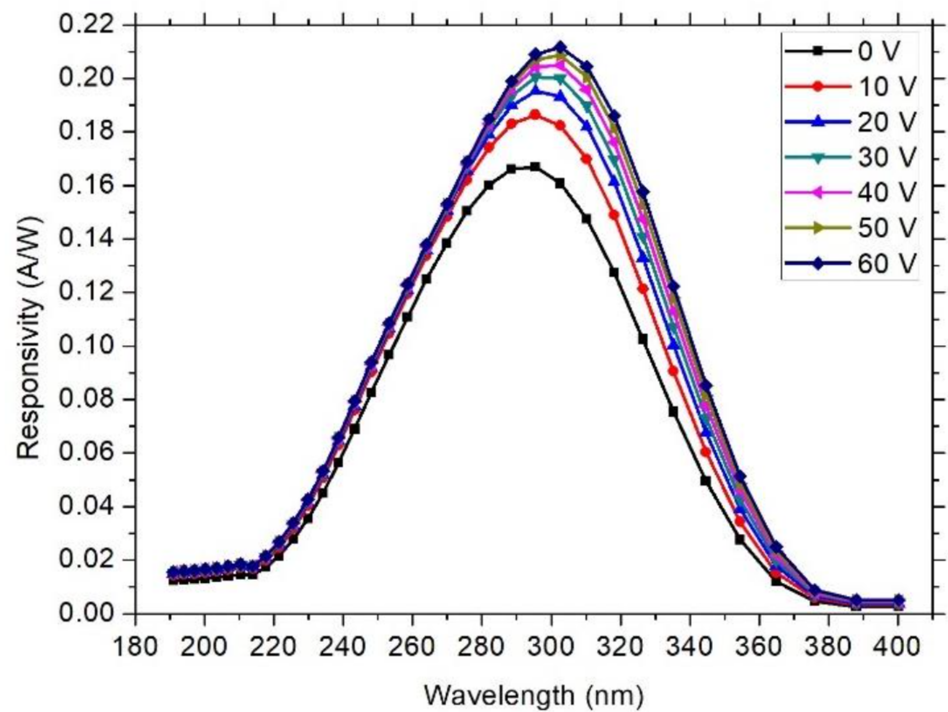

Figure 6. 4H−SiC UV p−i−n photodiode simulated spectral responsivities under different reverse biases, from 0 V to 60 V. A red−shift of about 6 nm of the responsivity peak wavelength is evident.

From Table 4, the responsivity peak increases from R = 0.168 A/W at 0 V to R = 0.212 A/W at 60 V. This last value corresponds to an EQE = 87.9%.

Table 4. Responsivities and external quantum efficiencies for different bias conditions for both experimental and simulation results.

Reverse Bias	Responsivity (R) Peak (A/W)		External Quantum Efficiency (EQE) (%) at Responsivity Peak	
	Experiments	Simulations	Experiments	Simulations
0 V	0.168	0.168	72.7	70.8
10 V	0.187	0.186	81.1	78.5
20 V	0.198	0.195	85.6	81.7
30 V	0.204	0.201	88.3	83.9
40 V	0.205	0.205	89.0	85.1
50 V	0.209	0.209	90.6	86.7
60 V	0.212	0.212	91.8	87.9

It is worth noting that, as bias increases, due to the consequent increase of the depletion region, the responsivity peak slightly shifts towards longer wavelengths (red−shift) [23], clearly visible also in Figure 6. A similar behaviour was observed experimentally. Moreover, it is evident that the responsivity curves show a widening on the right side. This is due to the longer penetration depth of photons as the wavelengths increase [5]. The responsivity sharp fall at short wavelengths is due, instead, to the smaller penetration depth of photons, which limit photogeneration within a small part of the front p−region.

Figures 7 and 8 show the electron concentration profiles along the vertical p−i−n UV photodiode structure for different reverse biases under illumination at the wavelength peaks and the corresponding widening of the depletion region as a function of the applied voltage.

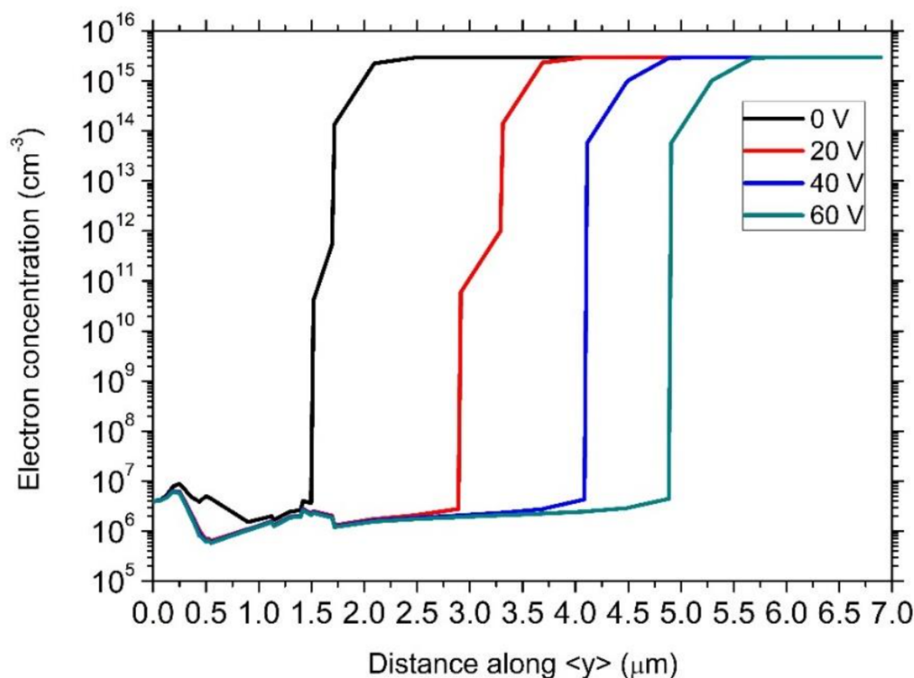

Figure 7. Electron concentration profile along the vertical <y> direction of the p−i−n photodiode at the responsivity peak wavelength from 0 V up to 60 V, in steps of 20 V.

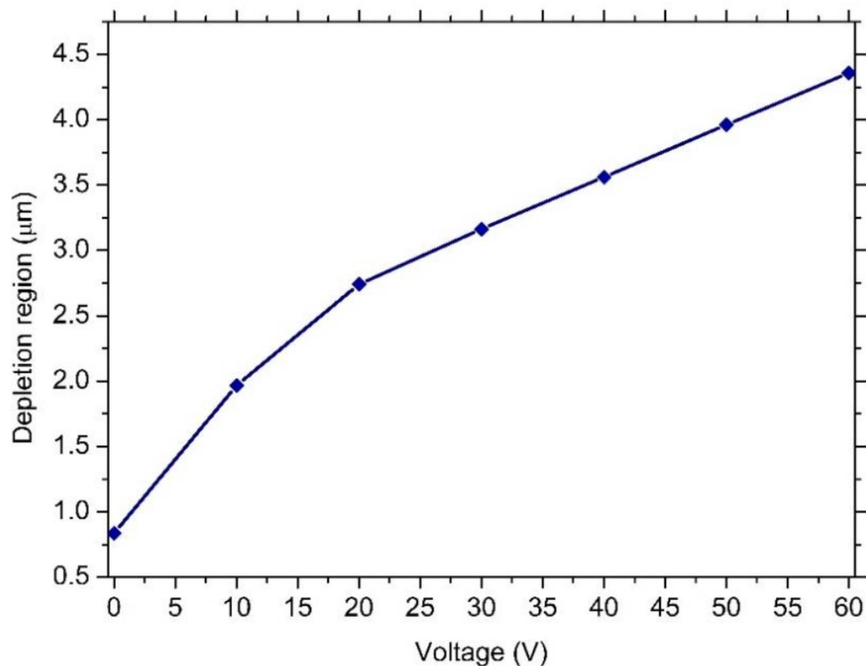

Figure 8. Simulated depletion region width under an optical beam at the responsivity peak wavelength as a function of the applied voltage.

In the same Table 4, the simulated results are reported, showing the good agreement in terms of R and EQE, a proof of our numerical model accuracy and reliability.

In Figure 9, a comparison between the simulated 4H−SiC UV p−i−n photodiode responsivities, at 0 V, 20 V, 40 V, and 60 V, and the corresponding experimental results, are shown.

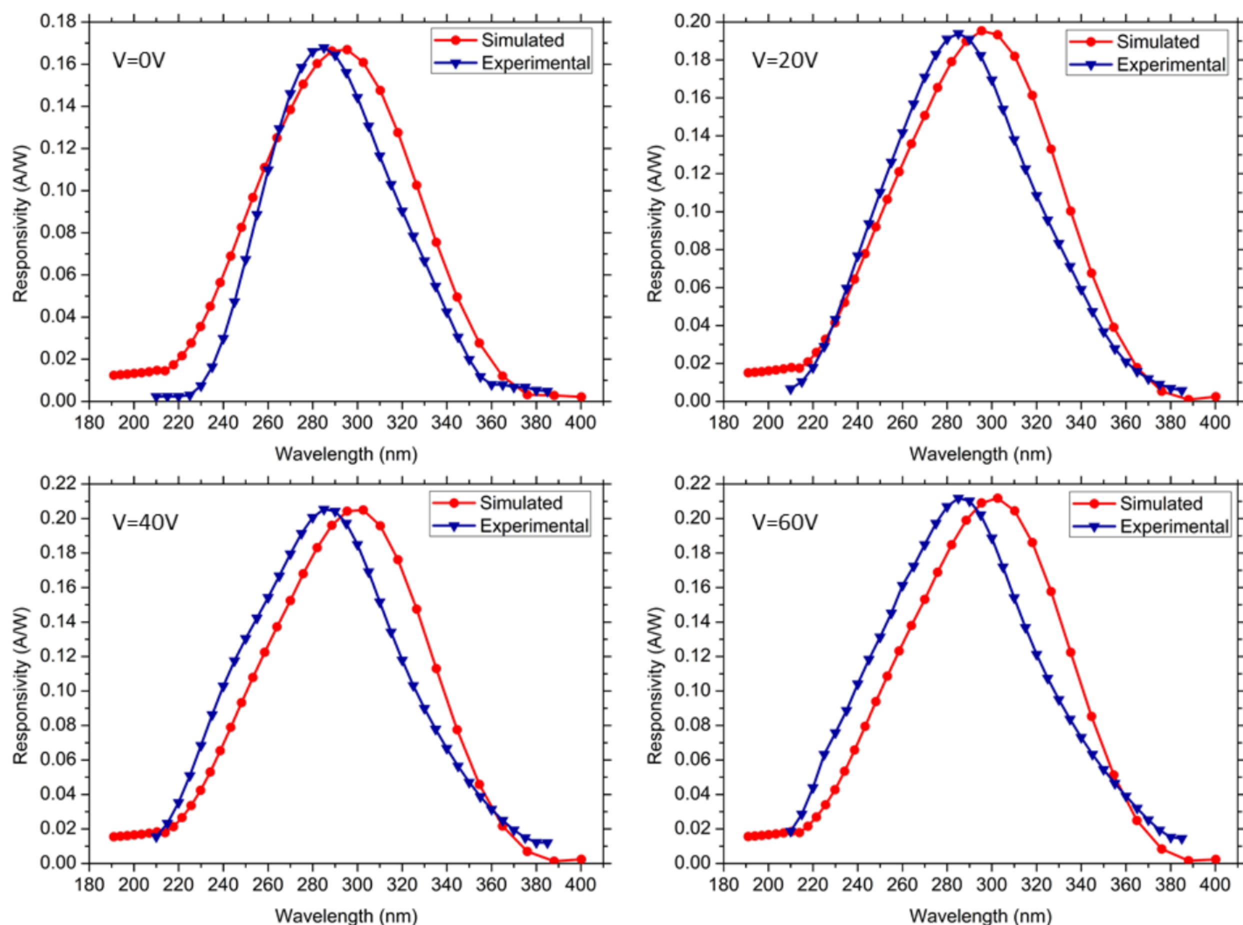

Figure 9. Comparison between the simulated 4H−SiC p−i−n UV photodiode responsivity and the experimental result at 0 V, 20 V, 40 V, and 60 V.

The spectral responsivity of the 4H−SiC p−i−n photodiode decreases gradually from R = 0.168 A/W at λ = 292 nm to about R = 3 mA/W at λ = 380 nm, at 0 V applied, whereas, at V = 60 V, the maximum of the responsivity increases by about 27% (R = 0.212 A/W) at a corresponding wavelength of λ = 298 nm. On the other hand, as the wavelength decreases, the responsivity, and hence the quantum efficiency, decreases, although the absorption coefficient of the 4H−SiC is higher at shorter wavelengths (Figure 4). This depends on the photon penetration length, which, in this wavelength range, becomes comparable with the dead zone due to the surface recombination [24,25].

5. Conclusions

The optical response of a high−performance 4H−SiC−based UV p−i−n photodiode was analysed by means of a numerical simulation model. The simulations were performed under different UV illuminations in a wavelength range from λ = 190 nm to 400 nm when a reverse bias, up to 60 V, was applied to the device.

The 4H−SiC photodiode exhibited a high value of responsivity, in particular at the wavelength of λ = 292 nm, R = 0.168 A/W, at 0 V. By increasing the reverse bias, the responsivity peak reaches the maximum value ever reported in the literature of R = 0.212 A/W, at 60 V. The corresponding quantum efficiency is about EQE = 71% and EQE = 88%, respectively.

The developed numerical model, used to compare the experiments, provided electro—optical results matching very well both theoretical and experimental data, validating therefore the goodness of our simulations.

Such a semiconductor device simulator may help the research community to understand and depict the physical processes in a 4H−SiC−based device and to make reliable predictions of the next−generation device behaviour. Simulations with properly selected calibrated parameters are, in fact, very useful for predictive parametric analysis of novel and more complex device structures.

Author Contributions: Conceptualization, S.R. and F.G.D.C.; methodology, S.R. and E.D.M.; validation, S.R. and F.G.D.C.; investigation, all; data curation, all; writing—original draft preparation, S.R. and E.D.M.; writing—review and editing, S.R. and F.G.D.C.; supervision, S.R. and F.G.D.C. All authors have read and agreed to the published version of the manuscript.

Funding: This research received no external funding.

Institutional Review Board Statement: Not applicable.

Informed Consent Statement: Not applicable.

Data Availability Statement: Not applicable.

Acknowledgments: Roberta Nipoti and the Clean Room staff of the CNR−IMM Unit of Bologna (Bologna, Italy) are thankfully recognized for providing the p−i−n diode and for stimulating discussions.

Conflicts of Interest: The authors declare no conflict of interest.

References

1. Morkoc, B.H.; Strite, S.; Gao, G.B.; Lin, M.E.; Sverdlov, B.; Burns, M. Large-band-gap SiC, III-V Nitride, and II-VI ZnSe-based Semiconductor Device Technologies. *J. Appl. Phys.* **1994**, *76*, 1363–1398. [CrossRef]
2. Monroy, E.; Omnès, F.; Calle, F. Wide−Bandgap Semiconductor Ultraviolet Photodetectors. *Semicond. Sci. Technol.* **2003**, *18*, R33. [CrossRef]
3. Megherbi, M.L.; Bencherif, H.; Dehimi, L.; Mallemace, E.D.; Rao, S.; Pezzimenti, F.; Della Corte, F.G. An Efficient 4H−SiC Photodiode for UV Sensing Applications. *Electronics* **2021**, *10*, 2517. [CrossRef]
4. Liu, H.D.; Guo, X.; McIntosh, D.; Campbell, J.C. Demonstration of Ultraviolet 6H−SiC PIN Avalanche Photodiodes. *IEEE Photonics Technol. Lett.* **2006**, *18*, 2508–2510. [CrossRef]
5. Sciuto, A.; Mazzillo, M.C.; Di Franco, S.; Mannino, G.; Badalà, P.; Renna, L.; Caruso, C. UV−A Sensor Based on 6H−SiC Schottky Photodiode. *IEEE Photonics J.* **2017**, *9*, 1–10. [CrossRef]
6. Cai, J.; Chen, X.; Hong, R.; Yang, W.; Wu, Z. High−Performance 4H−SiC−Based Pin Ultraviolet Photodiode and Investigation of Its Capacitance Characteristics. *Opt. Commun.* **2014**, *333*, 182–186. [CrossRef]
7. Burenkov, A.; Matthus, C.D.; Erlbacher, T. Optimization of 4H−SiC UV Photodiode Performance Using Numerical Process and Device Simulation. *IEEE Sens. J.* **2016**, *16*, 4246–4252. [CrossRef]
8. Sciuto, A.; Roccaforte, F.; Di Franco, S.; Raineri, V.; Bonanno, G. High Responsivity 4 H−Si C Schottky UV Photodiodes Based on the Pinch−off Surface Effect. *Appl. Phys. Lett.* **2006**, *89*, 081111. [CrossRef]
9. Zhou, Q.; Liu, H.D.; McIntosh, D.C.; Hu, C.; Zheng, X.; Campbell, J.C. Proton−Implantation−Isolated 4H−SiC Avalanche Photodiodes. *IEEE Photonics Technol. Lett.* **2009**, *21*, 1734–1736.
10. Ng, B.K.; Yan, F.; David, J.P.R.; Tozer, R.C.; Rees, G.J.; Qin, C.; Zhao, J.H. Multiplication and Excess Noise Characteristics of Thin 4H−SiC UV Avalanche Photodiodes. *IEEE Photonics Technol. Lett.* **2002**, *14*, 1342–1344. [CrossRef]
11. Chen, B.; Yang, Y.; Xie, X.; Wang, N.; Ma, Z.; Song, K.; Zhang, X. Analysis of Temperature−Dependent Characteristics of a 4H−SiC Metal−Semiconductor−Metal Ultraviolet Photodetector. *Chin. Sci. Bull.* **2012**, *57*, 4427–4433. [CrossRef]
12. Yang, S.; Zhou, D.; Lu, H.; Chen, D.; Ren, F.; Zhang, R.; Zheng, Y. High−Performance 4H−SiC Pin Ultraviolet Photodiode with p Layer Formed by al Implantation. *IEEE Photonics Technol. Lett.* **2016**, *28*, 1189–1192. [CrossRef]
13. Chen, X.; Zhu, H.; Cai, J.; Wu, Z. High−Performance 4H−SiC−Based Ultraviolet p−i−n Photodetector. *J. Appl. Phys.* **2007**, *102*, 24505. [CrossRef]
14. Della Corte, F.G.; Pezzimenti, F.; Nipoti, R. Simulation and Experimental Results on the Forward J–V Characteristic of Al Implanted 4H–SiC p–i–n Diodes. *Microelectron. J.* **2007**, *38*, 1273–1279. [CrossRef]
15. CNR−Institute for Microelectronics and Microsystem (IMM) of Bologna. Available online: https://www.bo.imm.cnr.it/unit/ (accessed on 31 March 2022).
16. SiC Materials, n−Type SiC Substrates. Available online: https://www.wolfspeed.com/products/materials/n$-$type$-$sic$-$substrates (accessed on 31 March 2022).
17. Pezzimenti, F.; Della Corte, F.G.; Nipoti, R. Experimental Characterization and Numerical Analysis of the 4H−SiC p–i–n Diodes Static and Transient Behaviour. *Microelectron. J.* **2008**, *39*, 1594–1599. [CrossRef]
18. Sze, S.M.; Li, Y.; Ng, K.K. *Physics of Semiconductor Devices*; John wiley & Sons: London, UK, 2021.

19. Caughey, D.M.; Thomas, R.E. Carrier Mobilities in Silicon Empirically Related to Doping and Field. *Proc. IEEE* **1967**, *55*, 2192–2193. [CrossRef]
20. Selberherr, S. *Analysis and Simulation of Semiconductor Devices*; Springer Science & Business Media: Berlin, Germany, 1984.
21. Zollner, S.; Chen, J.G.; Duda, E.; Wetteroth, T.; Wilson, S.R.; Hilfiker, J.N. Dielectric Functions of Bulk 4H and 6H SiC and Spectroscopic Ellipsometry Studies of Thin SiC Films on Si. *J. Appl. Phys.* **1999**, *85*, 8353–8361. [CrossRef]
22. Sridhara, S.G.; Devaty, R.P.; Choyke, W.J. Absorption Coefficient of 4H Silicon Carbide from 3900 to 3250 Å. *J. Appl. Phys.* **1998**, *84*, 2963–2964. [CrossRef]
23. Lioliou, G.; Mazzillo, M.C.; Sciuto, A.; Barnett, A.M. Electrical and Ultraviolet Characterization of 4H−SiC Schottky Photodiodes. *Opt. Express* **2015**, *23*, 21657–21670. [CrossRef]
24. Yan, F.; Xin, X.; Aslam, S.; Zhao, Y.; Franz, D.; Zhao, J.H.; Weiner, M. 4H−SiC UV Photo Detectors with Large Area and Very High Specific Detectivity. *IEEE J. Quantum Electron.* **2004**, *40*, 1315–1320.
25. Torvik, J.T.; Pankove, J.I.; Van Zeghbroeck, B.J. Comparison of GaN and 6H−SiC Pin Photodetectors with Excellent Ultraviolet Sensitivity and Selectivity. *IEEE Trans. Electron. Dev.* **1999**, *46*, 1326–1331. [CrossRef]